D2EHPA adsorption onto stearate-modified superparamagnetic nanoparticles: Development of a new material with potential hydrometallurgical applications

Farzad Firouzi, Ali Nemati, Sayed Khatiboleslam Sadrnezhaad *

Department of Materials Science and Engineering, Sharif University of Technology, Tehran, Iran

ABSTRACT

In the context of developing novel methodologies for hydrometallurgical separation of metal ions, the organic extractant-functionalized superparamagnetic nanoadsorbent materials have been recently welcomed as they simultaneously merge the critical advantages of solvent extraction and adsorption processes with an instant magnetic collectability feature. This work reports the preparation and characterization of D2EHPA-functionalized magnetite-based nanoadsorbents. The synthesized superparamagnetic nanoparticles are first chemically coated with stearic acid surfactant through a carboxylate chelating bidentate mechanism. Then, a monolayer D2EHPA extractant is physically adsorbed via Van der Waals interactions to the surface of stearate-modified nanoparticles. Aiming to get a deeper understanding of the process, it is comprehensively investigated from an adsorption viewpoint under various D2EHPA concentrations and temperatures. According to the statistical error analysis results, D2EHPA physisorption follows the Langmuir isotherm model, with a maximum adsorption capacity of 400.1 mg.g^{-1} at the optimum temperature of 25 °C. The process is exothermic ($\Delta H°_{ads} = -17.3$ kJ.mol^{-1}), decreases the system's disorder ($\Delta S°_{ads} = -46.6$ J.mol^{-1}.K^{-1}), and is thermodynamically favorable.

1. Introduction

In the hydrometallurgical production of metals, solvent extraction, and adsorption/ion exchange are the most widely-used techniques for separating and purifying metal ions. Despite exhibiting various advantages, the techniques suffer from some severe shortcomings. Solvent extraction is not efficient for dilute solutions and usually requires multiple stages. The entrainment of the organic phase into an aqueous solution and crud formation usually occurs in the solvent extraction systems leading to significant losses of the organic extractants, which are commonly expensive compounds with restricted accessibilities. Furthermore, the gravitational phase disengagement in the mixer-settler equipment is time-consuming and may take tens of minutes to complete. On the other hand, the ion exchange and adsorption techniques utilizing specific solid resins and other natural or synthesized adsorbent materials usually exhibit critical drawbacks related to metal loading capacity and subsequent desorption stage. Moreover, most ion exchange resins are exclusively supplied by a few manufacturers, resulting in their limited accessibility and high prices [1–4].

As adsorption is a heterogeneous surface-dependent process, the limited uptake capacity of adsorbent materials can be modified by reducing their size to the nano-scale and preparing so-called nano-adsorbents [5–7]. However, this would impose a new challenge for collecting and separating them from the aqueous solutions once the adsorption stage completes. Separating the nanoadsorbents through centrifugation, sedimentation, or filtration operations can become costly, tedious, or inapplicable on large scales. Magnetically-assisted chemical separation (MACS) based on employing magnetic adsorbent nanomaterials can be proposed as a simple and low-cost methodology to overcome the separation challenge [8,9]. In this technique, the loaded magnetic nanoadsorbents can instantly separate from the spent aqueous solution by applying an external magnetic field. In the context of magnetism, this requires a lack of coercivity and retentivity achieved when the nanoparticles are in the superparamagnetic state; i.e., each particle individually consists of a single magnetic domain. Thanks to high saturation magnetization, high permeability, low cost, and abundance, magnetite (Fe_3O_4) nanoparticles are generally known as an ideal candidate for the MACS technique, meeting their superparamagnetic

---

state for sizes smaller than about 30 nm [10–12].

The surface modification of superparamagnetic magnetite nanoparticles can improve their adsorption quality to generate potent nanoadsorbents for diverse applications [13–16]. A novel strategy in this context is to merge the solvent extraction technique with the adsorption process by utilizing the corresponding organic extractant compounds for functionalizing the magnetic nanoparticles. In this way, many vital shortcomings and limitations of the conventional solvent extraction technique can also be overcome. For instance, organic extractants would exhibit higher extraction efficiencies when present on the surface of nanoadsorbents due to better exposure to the aqueous solution rather than when they are distributed through the organic bulk solution as in the solvent extraction technique. Moreover, thanks to the exclusive properties of the organic extracting agents, the prepared nanoadsorbents can be adopted in hydrometallurgical systems to separate metal ions efficiently through selective adsorptions. In recent years, many common extracting agents, including organophosphorus acidic ones (e.g., D2EHPA [17–19], Cyanex 272 [18,19], Cyanex 301 [18–20], and P507 [21,22]) and solvating ones (primarily Cyanex 923 [23] and TBP [24,25]) have been employed for preparing the magnetic nano or microadsorbent materials. These novel extractant-functionalized adsorbents have been successfully utilized for hydrometallurgical extraction of critical metals such as rare earth elements, uranium, zirconium, rhenium, and molybdenum from bearing solutions with enhanced yields compared to many other conventional approaches [17–25].

Associated with functionalizing the superparamagnetic nanoparticles with extracting agents, the organic nature of the compounds hinders their direct attachment to the surface of bare hydrophilic magnetite nanoparticles. For this reason, the nanoparticles are usually first coated with a long-chain organic surfactant, and then, they could host the extractants. Indeed, the organic segment of extracting agent molecules anchors firmly through Van der Waals interactions in the upstanding hydrocarbon chains of the surfactant on the surface of nanoparticles. It is unanimously believed that this process occurs via the physisorption mechanism [18,19,23–26]. Although the involved physical forces may not be as strong as chemical ones, they are still adequately greater than the desorption forces endowed on the molecules by their thermal energy. However, the intended functionalization process has never been studied from an adsorption process viewpoint in any previous research on preparing extractant-functionalized nanoadsorbents. Thus, the corresponding aspects, including the expressive adsorption isotherm model, surface properties, and valuable adsorption thermodynamics data, have remained ambiguous and unknown.

Long-chain fatty acids are generally known as one of the most widely used types of organic surfactants for initial surface modification of bare nanoparticles; among them, oleic acid stands out [26–29]. However, oleic acid is an unsaturated fatty acid whose alkyl chain bends at the position of the *cis* double bond. This kinked structure prevents the molecules from packing closely either in bulk state or on the surface attached. On the other hand, the straight alkyl chain of saturated fatty acids packs much tighter and, thus, can possess stronger Van der Waals intermolecular forces [30,31]. In support of this claim, one can consider stearic acid, as the saturated counterpart of oleic acid, with a 17 carbon atoms long alkyl chain in which a single bond replaces the carbon double one. The melting point of stearic acid (70 °C) is significantly higher than that of oleic acid (14 °C), as higher thermal energy is required to loosen the involved physical intermolecular bonds between alkyl chains. Thus, substituting oleic acid surfactant with its saturated counterpart is expected to strengthen the adhesion of the extractant molecules through the resultant stearate layer. The stearic acid layer's more effective packing density may also better protect magnetite's core against high acidity solutions. Interestingly, as far as the authors know, the utilization of stearic acid in the context of preparing extractant-functionalized nanoadsorbents has not been reported yet.

The present study reports the development of superparamagnetic D2EHPA-functionalized nanoadsorbents suitable for separation and purification applications in hydrometallurgical systems. In brief, magnetite nanoparticles are first synthesized via the chemical co-precipitation method, then coated with stearic acid, and finally functionalized with D2EHPA extractant. The process is investigated for various concentrations of the extractant compound at three different temperatures to shed light on the adsorptive features of the final functionalization section and corresponding optimization. A comprehensive statistical analysis based on the non-linear regression method is performed to evaluate the adsorption data toward various equilibrium isotherm models and determine the one that best describes the process. Accordingly, valuable information on the mechanism and thermodynamics of the nanoadsorbents preparation is extracted.

2. Materials and methods

2.1. Chemicals

The chemical reagents required for synthesis and surface modification of magnetite nanoparticles, including ferrous chloride tetrahydrate ($FeCl_2 \cdot 4H_2O$), ferric chloride hexahydrate ($FeCl_3 \cdot 6H_2O$), stearic acid ($C_{17}H_{35}COOH$), ammonia solution (NH_4OH, 25 %), and anhydrous ethanol (C_2H_5OH) were purchased from Merck, Germany. The organic extractant di-(2-ethylhexyl) phosphoric acid (D2EHPA, $(C_8H_{17}O)_2POOH$)) used for functionalizing the final nanoadsorbents was provided from Fluka, Switzerland. All the chemicals were of analytical grade and used as received without further purification. Milli-Q water (18.2 MΩ.cm resistivity) was utilized to prepare the aqueous solutions and rinse the laboratory glassware.

2.2. Experimental procedure

2.2.1. Synthesis of magnetite nanoparticles

Magnetite nanoparticles were synthesized via the chemical co-precipitation of ferrous and ferric ions in an alkaline medium. In a typical synthesis procedure, 50 mL of 0.1 M ferrous solution was added to 50 mL of 0.2 M ferric solution, both prepared through solvating the corresponding chloride precursors in Milli-Q water, to attain a $2Fe^{3+}/Fe^{2+}$ molar ratio. The solutions were mechanically mixed and degasified in a three-necked balloon under an inert nitrogen atmosphere, which was maintained throughout the process. Subsequently, the temperature was raised to 80 °C, and the pH was increased to about 9 by gradually adding ammonia solution. In the same circumstances, the solution was kept mixing for 30 min while the formation of magnetite nanoparticles was evidenced by turning its yellowish color into black. After terminating the process and letting the solution cool down to room temperature, the resultant precipitate was collected by a NdFeB magnet tool and washed with several portions of ethanol and degasified Milli-Q water to attain a neutral pH. At last, the magnetite nanoparticles were vacuum-dried overnight and stored.

2.2.2. Surface modification with stearic acid

Due to the insolubility of long-chain fatty acids in aqueous solutions, the surface modification process of magnetite nanoparticles with stearic acid was conducted in an ethanol medium. For this purpose, the synthesized nanoparticles were added to a saturated solution of stearic acid in ethanol (0.1 g for every 100 mL solution), and the suspension was probe sonicated for 60 min. Then, the supernatant was decanted, and the stearic acid-coated magnetite nanoparticles (SA-MNP) were rinsed three times with ethanol to remove any free stearic acid remaining on the surface, and finally vacuum-dried to a constant weight and stored.

2.2.3. Functionalization with organic extractant

The surface functionalization process through the adsorption of organic extractant onto the SA-MNP consisted of two consecutive stages. In the first stage, 0.1 g of the reserved SA-MNP was added to 100 mL batches of D2EHPA solution of varying concentrations diluted in ethanol

and probe sonicated for 20 min. This stage aimed to deagglomerate the nanoparticles to achieve a homogeneous dispersion and their primary functionalization.

In order to investigate the effect of temperature on the equilibrium adsorption of D2EHPA onto the surface, the process conduction at different temperatures of 25, 40, and 55 °C was considered. For this purpose, the process vessel was transferred to a water bath for exact temperature control. The second stage of functionalization was followed by mechanical stirring of the suspension in the water bath at a certain temperature for 60 min. Preliminary experiments confirmed that the duration was sufficient for attaining equilibrium at all the intended temperatures. At last, the resultant D2EHPA-functionalized magnetite nanoparticles (D2EHPA-MNP) were collected utilizing a NdFeB magnet tool, washed three times with ethanol (of the same temperature as the intended process) to remove any free D2EHPA molecules, and vacuum-dried to a constant weight.

2.2.4. Characterization

The X-ray diffraction (XRD) patterns were acquired over the 2θ scan range from 5° to 80° by a PANalytical X'Pert PRO MPD diffractometer, with Cu-Kα radiation, and the subsequent phase analysis was carried out utilizing the X'Pert Highscore Plus program. A TESCAN MIRA3 LMU microscope was used to record field-emission scanning electron microscopy (FE-SEM) images. The magnetic response of nanoparticles was measured at room temperature with a Kavir MDKB vibrating sample magnetometer (VSM) up to 5000 Oe applied magnetic field. A Perkin-nElmer Spectrum RX I spectrometer equipped with NaCl Windows was employed to perform the Fourier Transform Infrared Spectroscopy (FT-IR) through the KBr method in the spectral range from 400 to 4000 cm^{-1} with a resolution of 1 cm^{-1}. Thermogeravimetric analysis (TGA) was carried out in a Mettler Toledo TGA/DSC 1 STARe System device with the thermal program from 25 to 800 °C via a constant temperature rise of 5 °C/min in an inert atmosphere of N_2 (flow rate of 50 mL/min).

In the context of adsorption studies, the loading capacity of adsorbent materials is typically calculated based on the mass balance principle, according to the initial and equilibrium concentrations of the adsorbate in the containing solution [17–25]. This procedure is convenient for the adsorption of aqueous constituents, such as metal ions, that can be measured by elemental analysis or spectroscopic methods. However, due to some operational restrictions, direct determination of the organic D2EHPA extractant through the prevalent analytical techniques was challenging, imposing the adoption necessity of an applicable methodology for obtaining the corresponding adsorption capacity. In this regard, a simple gravimetric strategy based on the exact weighting of the intended adsorbent material (SA-MNP) just before and after D2EHPA adsorption was employed in the present study. The experiments were carried out in triplicate with a 0.0001 g weighting precision. The adopted classical gravimetric strategy seems useful specifically for relatively high molecular weight adsorbates, including organic extractants (D2EHPA = 322 g.mol^{-1}).

3. Theoretical framework

3.1. Adsorption isotherm models

The nature and mechanism of an adsorption process can be well-studied by adsorption isotherm models, which coordinate the equilibrium uptake capacities per unit weight of adsorbent q_e (mg.g^{-1}) with the equilibrium concentrations of adsorbate C_e (mol.L^{-1}) at a constant temperature [32,33]. Langmuir, Freundlich, Temkin, and Dubinin-Radushkevich are the best-known isotherm models being considered in the present study. As the principles and exclusive details are widely available in the literature, their relations (Equations (1) to (6)) and corresponding parameters are just summarized in Table 1.

Table 1
Adsorption isotherm models' definition and parameters.

Isotherm model	Equation		Parameters
Langmuir	$q_e = \dfrac{q_m K_L C_e}{1 + K_L C_e}$	(1)	K_L: Langmuir constant q_m: Maximum theoretical adsorption capacity
Freundlich	$q_e = \dfrac{1}{K_F C_e^{\overline{n}}}$	(2)	K_F: Freundlich constant $1/n$: Freundlich constant (related to the adsorption intensity)
Temkin	$q_e = \dfrac{RT}{b}\ln(K_T C_e)$ $B = \dfrac{RT}{b}$	(3) (4)	K_T: Temkin constant b: Temkin constant (related to the adsorption energy) B: Adsorption energy
Dubinin-Radushkevich	$q_e = q_m\exp\left(-K_{D-R}\varepsilon^2\right)$ $\varepsilon = RT\ln\left(1 + \dfrac{1}{C_e}\right)$	(5) (6)	K_{D-R}: Dubinin-Radushkevich constant q_m: Maximum theoretical adsorption capacity ε: Adsorption potential (based on the Polanyi's potential theory)

3.2. Statistical error analysis

The isotherm models' fitting to the experimental adsorption results were statistically assessed through non-linear regression utilizing the 'SOLVERSTAT' add-in by MS Excel [34]. Various error functions including root-mean-square error (RMSE), the sum of the squares of the errors (ERRSQ), Marquardt's percent standard deviation (MPSD), average relative error (ARE), Chi-square analysis (χ^2), and hybrid fractional error function (HYBRID) were selected to quantify the difference between the values of experimental data and those predicted by the models (refer to the Supplementary Information for the corresponding calculation formulae). The lower the error functions' values, the better the quality of the predictive model fitting.

Since different sets of isotherm parameters may be produced according to the type of error functions considered, all the error results should be combined by calculating a so-called 'sum of normalized errors' (SNE) for each parameter set [35–37]. The minimal SNE value belongs to the optimum parameter set for the intended isotherm model. The detailed calculation method of the SNE is provided in the Supplementary Information.

3.3. Adsorption thermodynamics

Thermodynamic aspects of the nanoadsorbents' preparation, i.e., the extractant adsorption onto the surface of stearate-modified magnetite nanoparticles, can be well studied by determining the relevant parameters. The standard Gibbs free energy change ($\Delta G°$) during the adsorption process is fundamentally expressed in terms of the adsorption equilibrium constant (K_{ads}) according to Equation (7):

$$\Delta G° = -RT\ln K_{ads} \tag{7}$$

where R and T represent the universal gas constant (8.314 J.mol^{-1}.K^{-1}) and absolute temperature (K), respectively. By applying the concepts of standard adsorption enthalpy and entropy changes ($\Delta H°_{ads}$ and $\Delta S°_{ads}$) to Equation (7), the well-known Van't Hoff relation (Equation (8)) is obtained:

$$\ln K_{ads} = \frac{-\Delta H°_{ads}}{RT} + \frac{\Delta S°_{ads}}{R} \tag{8}$$

Having the values of adsorption equilibrium constant at various temperatures and by constructing the plot of $\ln K_{ads}$ versus $1/T$, based on the Van't Hoff relation, it is possible to obtain the thermodynamic parameters. Indeed, $\Delta H°_{ads}$ and $\Delta S°_{ads}$ are calculated from the slope and intercept of the linear Van't Hoff plot, respectively. It is worth

mentioning that the dimensionless equilibrium constant (K_{ads}) for the adsorption system can be obtained from the best-fitted isotherm model's constant [38,39].

4. Results and discussion

4.1. Characterization of nanoadsorbents

The XRD patterns of the as-synthesized nanoparticles and those coated with stearic acid and further functionalized with D2EHPA extractant are depicted in Fig. 1(a). The presence of sharp Bragg peaks evidences the crystalline nature of the nanoparticles. The identified peaks are the characteristic of the single-phase magnetite inverse spinel crystalline structure according to the Joint Committee for Powder Diffraction Standards (JCPDS) card no. 19–0629 for Fe_3O_4. The absence of additional peaks in all XRD patterns confirms that the single-phase magnetite nanoparticles are chemically stable and have not been oxidized during the preparation procedure of the nanoadsorbents.

The average crystallite size of nanoparticles, D, can be derived by applying the Debye-Scherrer relation, according to Equation (9):

$$D = \frac{K\lambda}{\beta\cos\theta} \tag{9}$$

where K is the shape factor (usually 0.9), λ is the wavelength of anode X-ray radiation (Cu-Kα = 0.15406 nm for copper anode), and β represents the full width broadening estimated at half maximum intensity (FWHM) of the peak corresponding to its Bragg angle, θ. Accordingly, the magnetite nanoparticles' average crystallite size is calculated to be 14.8 nm.

Fig. 1(b) illustrates the field-emission scanning electron microscopy (FE-SEM) image of the synthesized magnetite nanoparticles. It can be observed that despite agglomeration, occurring unavoidably during the specimen preparation for microscopy, the intended nanoparticles are almost spherical in geometrical shape with a reasonably narrow normal size distribution. Based on statistical analysis using ImageJ software, the average size of nanoparticles is estimated to be 15.3 ± 1.7 nm. The size agrees well with the crystallite size calculated according to the Debye-Scherrer equation from the XRD patterns, implying a single-domain structure.

Alongside favorable chemical properties and capabilities, appropriate magnetic behavior is required for magnetic nanoadsorbents to ensure their practical application. They should be able to repeatedly disperse nicely through the aqueous solution and subsequently undergo an immediate magnetic separation. This necessity is ideally fulfilled by a value of zero coercivity, the absence of retentivity, and high permeability, which are the fundamental characteristics of superparamagnetic nanoparticles. Superparamagnetism implies that each particle is individually constituted of a single magnetic domain, in which the magnetic moments are quickly oriented in the external magnetic field, and this orientation completely collapses when the field is removed.

The prepared single-domain nanoparticles are expected to be in the superparamagnetic state since they are smaller than the magnetite's critical size ($\sim$30 nm). This expectation can be further validated through the VSM analysis. Fig. 2 represents the magnetic responses of pristine magnetite nanoparticles (MNP) together with those coated with stearic acid (SA-MNP) and further functionalized with D2EHPA extractant (D2EHPA-MNP). The non-cyclic appearance of all magnetization curves visually implies the absence of hysteresis loss. Moreover, the values of both coercivity and retentivity are minimal for all samples. These facts directly confirm that the intended nanoparticles are in the superparamagnetic state, as pointed out previously.

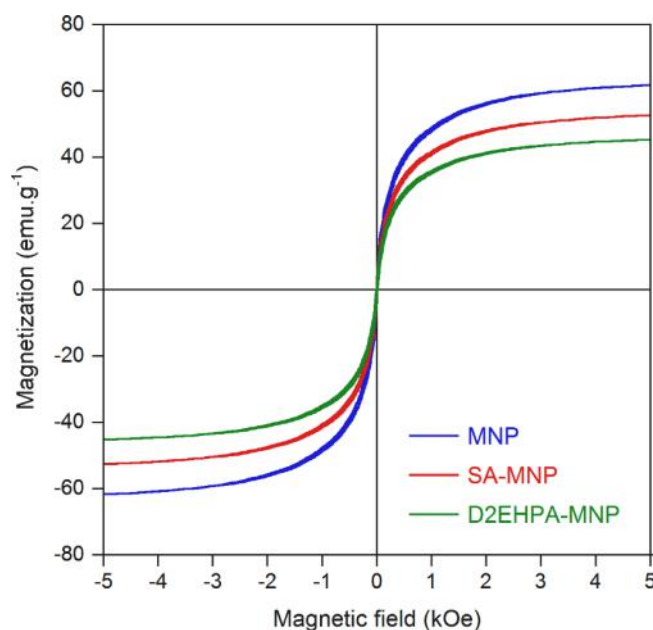According to Fig. 2, the saturation magnetization of the magnetic

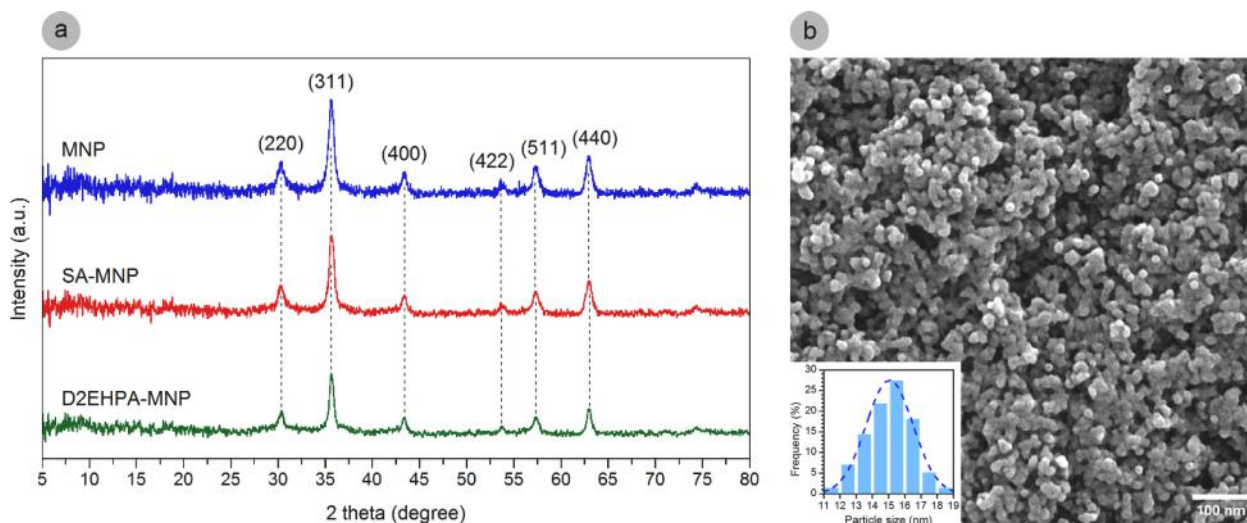**Fig. 2.** Magnetization curves of MNP, SA-MNP, and D2EHPA-MNP.

Fig. 1. (a) XRD patterns of MNP, SA-MNP, and D2EHPA-MNP. (b) FE-SEM image of the synthesized magnetite nanoparticles.

nanoparticles diminishes from 62 emu.g^{-1} for MNP to 53 and further to 48 emu.g^{-1} for SA-MNP and D2EHPA-MNP, respectively. Indeed, these successive drops in saturation magnetization result from non-magnetic organic layers (i.e., stearic acid and D2EHPA) surrounding the magnetite core, which weaken the magnetic effectiveness of the corresponding nanoparticles. The thicker the organic coating layer, the lower the magnetic response against an external magnetic field. Nevertheless, the final saturation magnetization for D2EHPA-functionalized nanoadsorbents still suffices for their instant magnetic separation from the raffinate using a simple magnet tool.

The surface modification of magnetite nanoparticles with stearic acid and their further functionalization with D2EHPA extractant can be comprehensively studied via FT-IR spectroscopy. It is also possible to shed light on the types of interactions involved (physical or chemical) and discuss the relevant mechanisms by analyzing the associated chemical bonds in this technique. Fig. 3 presents the FT-IR spectra of pure stearic acid and the magnetite nanoparticles coated with this fatty acid (SA-MNP) in section (a), together with those of pure D2EHPA and the nanoadsorbents functionalized with this organic extractant (D2EHPA-MNP) in section (b).

According to the pure stearic acid spectrum presented in Fig. 3(a), two bands at 1706 and 1297 cm^{-1} positions are attributed to the characteristic C=O and C—OH stretching vibrations of the available carboxyl group, respectively. Furthermore, the in-plane and out-of-plane bending vibrations of the O—H bond associated with this functional group can be correspondingly identified at 1464 and 933 cm^{-1} wavenumbers. The alkane chain of the structure is evidenced by two characteristic bands located at 2856 and 2924 cm^{-1}, corresponding to the symmetric and asymmetric stretching vibrations of C—H, respectively.

The FT-IR spectra corresponding to the magnetite-based samples present a strong characteristic band at 580 cm^{-1}, assigned to the Fe—O

stretching vibration. In the context of SA-MNP, the appearance of two C—H characteristic bands (2856 and 2924 cm^{-1}) in the intended spectrum (Fig. 3(a)) confirms the presence and permanence of stearic acid molecules on the surface of magnetite nanoparticles. However, the characteristic bands corresponding to the carboxyl group of the fatty acid structure (1706, 1464, 1297, and 933 cm^{-1}) are clearly absent in this spectrum, implying that the functional group has been chemically changed during the coating process. On the other hand, two new bands are observed at 1421 and 1524 cm^{-1}, which can be attributed to the carboxylate's (O—C—O) symmetric and asymmetric stretching vibrations, respectively. These results disclose that a monolayer stearic acid is chemically bonded to the surface of magnetite nanoparticles by carboxylate interactions.

The mechanism of chemical interaction between the carboxylate head and the surface of magnetite nanoparticles can be generally categorized into three types: monodentate, bridging bidentate, and chelating bidentate, as schematically depicted in Fig. 4. The existing mechanism type can be identified through the wavenumber separation between carboxylate's characteristic symmetric and asymmetric stretching vibrations, $\Delta\nu(COO^-)$, in the FT-IR spectrum. Accordingly, a $\Delta\nu(COO^-)$ value within the 200–320 cm^{-1} range implies the monodentate interaction (Fig. 4(a)), while a value between 140 and 190 cm^{-1} refers to the bridging bidentate mechanism (Fig. 4(b)). Specifically, when the $\Delta\nu(COO^-)$ value is less than 110 cm^{-1}, as occurred in the present study (1524–1421 = 103 cm^{-1}), the carboxylate covalently interacts with the surface of magnetite nanoparticles via the chelating bidentate mechanism (Fig. 4(c)) [28,29].

Referring to the first FT-IR spectrum in Fig. 3(b), the characteristic stretching vibration bands of D2EHPA corresponding to P=O, P—O—C, and P—O—H are indexed at 1230, 1033, and 2324 cm^{-1}, respectively. The C—H bonds associated with the alkane chains of the structure can be recognized through their symmetric and asymmetric stretching vibration bands correspondingly present at 2866 and 2960 cm^{-1} wavenumbers. Furthermore, two bands around 1464 and 1381 cm^{-1} are attributed to the C—H deformation vibrations due to more than one CH$_3$ group on a carbon atom. D2EHPA molecules usually tend to pairwise interact with each other via strong hydrogen bonding to form dimers. In this context, the band located at 1694 cm^{-1} is representative of the O—H intermolecular hydrogen bonds of dimeric D2EHPA.

In addition to the Fe—O characteristic band (580 cm^{-1}), all characteristic vibration bands of D2EHPA extractant are correspondingly present in the FT-IR spectrum of D2EHPA-MNP (Fig. 3(b)), confirming the successful attachment of D2EHPA molecules onto the surface of stearic acid-coated magnetite nanoparticles (SA-MNP). Specifically, the characteristic P=O and P—O—H vibration bands of D2EHPA (1230 and 2324 cm^{-1}) remain unchanged in the D2EHPA-MNP spectrum. This fact indicates that no chemical interaction occurs during the

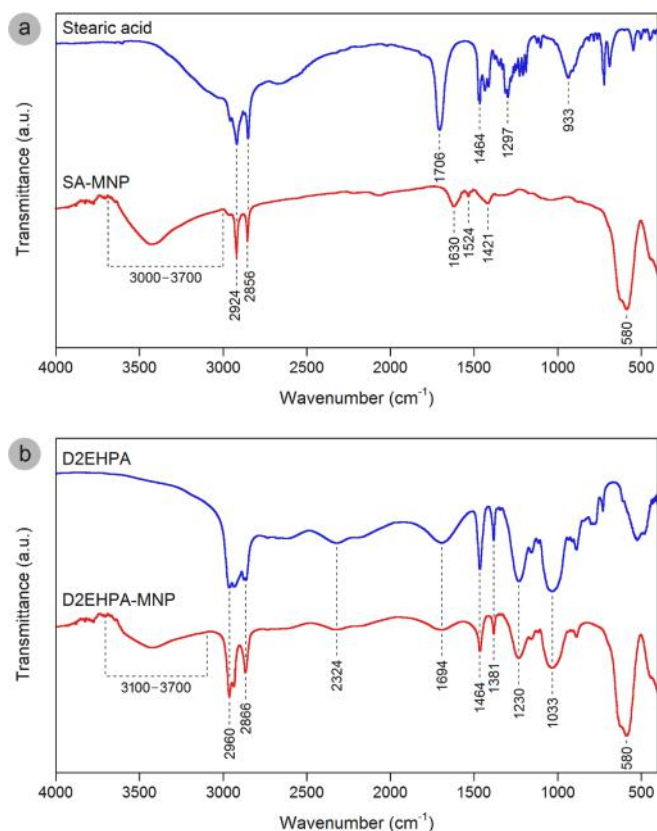**Fig. 3.** FT-IR spectra of (a) stearic acid and SA-MNP and (b) D2EHPA and D2EHPA-MNP.
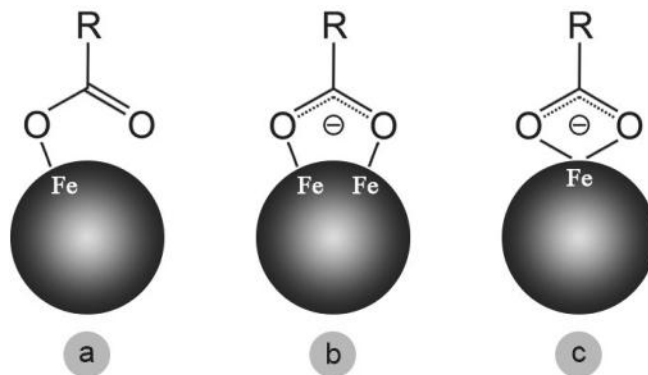

Fig. 4. Possible mechanisms of the carboxylate's chemical interaction with the surface of magnetite nanoparticles: (a) monodentate, (b) bridging bidentate, and (c) chelating bidentate.

functionalization process, and the organic extractant preserves its extractive capability for further hydrometallurgical applications (i.e., extraction of metal ions).

It is also worth pointing out that the broadband appearing around the 3000–3700 cm^{-1} wavenumber range in the magnetite-based FT-IR spectra is assigned to the O—H stretching vibration of the hydroxyl group associated with the water molecules being adsorbed from the atmospheric moisture during specimen preparation. Accordingly, the bending mode vibration of the water's H—O—H hydroxyl groups can be identified through the band located at 1630 cm^{-1} in the SA-MNP spectrum, being merged with the adjacent band in the D2EHPA-MNP one. Meanwhile, the discussed hydroxyl group differs from the previously mentioned O—H intermolecular hydrogen bonds in D2EHPA dimers.

In order to get quantitative information about the organic contents of the surface-modified nanoparticles, their thermal stabilities can be investigated using thermogravimetric analysis (TGA). Fig. 5 illustrates TGA curves representing temperature-dependent mass changes for SA-MNP and D2EHPA-MNP samples. The extent and temperature range of the corresponding mass change stages have also been provided in the curves.

Non-uniform mass changes with temperature rise observed in the TGA curves suggest the decomposition/volatilization/desorption of the organic compounds present on the intended nanoadsorbent materials. The mass changes occur through four stages for the SA-MNP, while the D2EHPA-MNP curve exhibits one more stage due to its further functionalization with the organic extractant compound.

According to Fig. 5, an initial mass loss of a maximum of 2.0 % is observed below 152 °C for the samples, which is assigned to evaporation of any remaining solvent (i.e., water and/or ethanol) used in the synthesis, coating, or functionalization processes. In curve (a) corresponding to the SA-MNP, a significant mass loss of 10.6 % is observed in the range of 152–488 °C, which can be attributed to the desorption and decomposition of the chemisorbed stearate group. Most likely due to the same reason, the similar mass loss stage of 7.1 % can be observed at temperatures between 322 and 484 °C in the curve (b) corresponding to the D2EHPA-MNP. In this context, increasing the decomposition temperature of the stearate group in the D2EHPA-functionalized nanoadsorbents can be correlated with the presence of an additional layer of the organic extractant on their outer surface which postpones the stearate's decomposition by playing a protective role.

Furthermore, the D2EHPA-MNP experiences an additional mass loss of 20.8 % in the temperature range of 119–322 °C. Being absent in the SA-MNP curve, this stage is directly ascribed to desorption and subsequent decomposition of the organic D2EHPA extractant physisorbed onto the SA-MNP surface. This interpretation is confirmed by considering the decomposition point of D2EHPA (240 °C), which lies within the temperature range of the intended stage.

It is worth mentioning that the probable incomplete decomposition of the involved organic constituents (stearate group and D2EHPA molecules) during the previous stages may have left some residual carbon derivatives on the surface of nanoparticles. Therefore, the slight mass rise for temperatures higher than about 485 °C observed in both TGA curves may be attributed to the adsorption of nitrogen (utilized inert gas for the analysis) on these carbonaceous residues. The greater extent of mass rise for D2EHPA-MNP (2.8 %), compared to the SA-MNP (0.9 %), can be assigned to the generation of more carbon derivatives due to additional decomposition of the organic extractant compound, which consequently increases the adsorption amount of nitrogen gas. However, this would not last for temperatures over about 700 °C since the thermal decomposition and oxidation of the carbonaceous residues at higher temperatures would finally lead to the emission of CO$_x$ gases (supplying the required oxygen from magnetite structure) and occurring final mass loss stage of the TGA curves.

4.2. D2EHPA adsorption studies

Fig. 6 represents the equilibrium adsorption of D2EHPA in terms of its uptake capacity per unit weight of the SA-MNP as adsorbent for various equilibrium concentrations of the extractant at different temperatures of 25, 40, and 55 °C. As expected, increasing the extractant concentration leads to its higher loading extent. In this regard, the equilibrium adsorption rises steeply for about 0.75 M and then gradually moves toward the saturation state for higher concentrations. Moreover, the adsorption proceeds more efficiently at lower temperatures revealing the process's exothermic nature. The obtained equilibrium data should be evaluated based on the adsorption isotherm models to shed light on dark aspects of the D2EHPA molecules' interaction with the stearate-modified surface of magnetite nanoparticles.

The results of non-linear regression analysis for Langmuir, Freundlich, Temkin, and Dubinin- Radushkevich isotherm models fitting to the experimental data for D2EHPA extractant adsorption onto the stearate-modified surface of magnetite nanoparticles (SA-MNP) are provided in Tables S1 to S4 of the Supplementary Information.

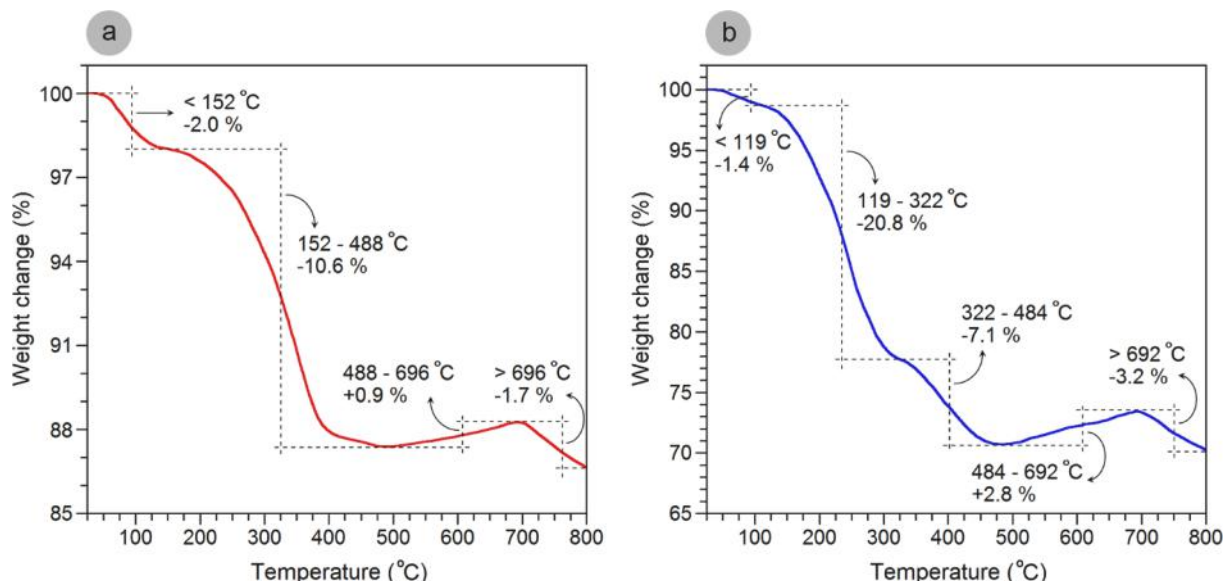In the context of Langmuir isotherm, the SNE values (Table S1)

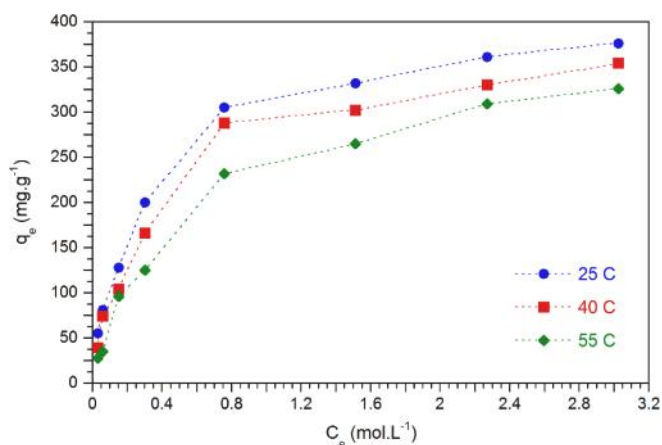**Fig. 5.** TGA curves corresponding to (a) SA-MNP and (b) D2EHPA-MNP.

Fig. 6. Equilibrium adsorption of D2EHPA onto SA-MNP (for preparing D2EHPA-MNP) at 25, 40, and 55 °C.

disclose that the HYBRID parameter sets produce the best overall fits for D2EHPA adsorption onto SA-MNP at all three temperatures studied. The Langmuir constant K_L decreases from 3.718 ± 0.389 to 2.987 ± 0.446 and finally 1.956 ± 0.236 L.mol^{-1} by the process temperature rise from 25 to 40 and 55 °C, respectively. For this temperature sequence, the maximum adsorption capacity q_m also undergoes a descending trend from 400.1 ± 10.6 to 382.3 ± 15.2 and then 373.1 ± 13.6 mg.g^{-1}, inferring the exothermic nature of the corresponding adsorption process.

According to the Langmuir isotherm, the adsorption favorability can be evaluated in terms of the dimensionless separation factor (R_L) parameter defined by Equation (10). Fig. 7 represents this parameter calculated for various initial concentrations of D2EHPA at the intended temperatures. The R_L values less than 1 and greater than 0 for all the concentrations and temperatures imply that the investigated adsorption process is utterly favorable. As expected, the favorability improves by increasing the initial concentration of the extractant at lower temperatures.

$$R_L = \frac{1}{1 + K_L C_0} \tag{10}$$

Based on the SNE values for Freundlich isotherm (Table S2), the HYBRID parameter sets result in the closest fits to the adsorption data at all temperatures. Accordingly, temperature elevation from 25 to 40 and 55 °C would decrease the Freundlich constant K_F from 270.786 ± 13.980 to 243.366 ± 14.756 and 206.790 ± 12.617 mg.g^{-1}.(L.mol^{-1})$^{1/}$
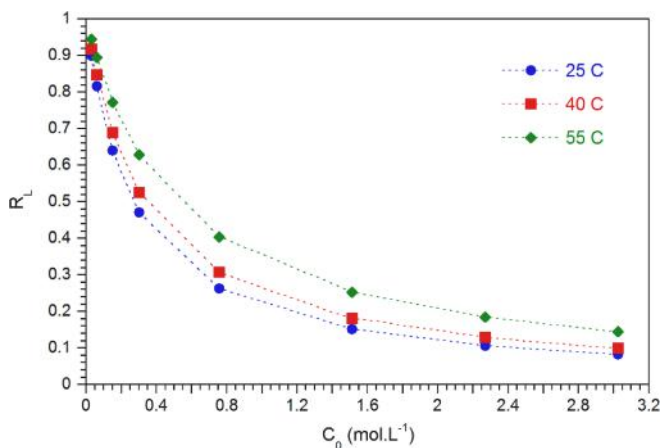

Fig. 7. Separation factor (R_L) of D2EHPA adsorbed onto SA-MNP at 25, 40, and 55 °C.

n, respectively. The $1/n$ constant is also determined as 0.389 ± 0.051, 0.426 ± 0.061, and 0.505 ± 0.064 correspondingly at the as-mentioned temperatures. The variation trends of the Freundlich constants (K_F and $1/n$) imply drops in the adsorption capacity and intensity by temperature rising. Moreover, less than unity values obtained for the $1/n$ constant indicate that D2EHPA adsorption onto the surface of SA-MNP is quite favorable.

For Temkin isotherm, according to the SNE values (Table S3), the best overall fits to the adsorption data are produced by χ^2 parameter sets at both 25 and 40 °C, and by HYBRID one at 55 °C. Temperature rise from 25 to 40 and 55 °C diminishes the Temkin constant K_T from 62.504 ± 13.822 to 53.266 ± 14.336 and finally 38.821 ± 10.809 L.mol^{-1}, respectively, which indicates the lowering of bonding energy. The B parameter, expressing the adsorption energy, also undergoes a descending trend from 71.639 ± 4.405 to 68.106 ± 5.307 and then 62.807 ± 5.504 J.mol^{-1} correspondingly for the as-mentioned temperatures. Therefore, it can be concluded that the process of D2EHPA adsorption onto SA-MNP is more efficient at lower temperatures due to more energy release. The obtained energy values (< 20 kJ.mol^{-1}) also imply the physical nature of the intended adsorption, as expected.

The SNE values for the Dubinin-Radushkevich isotherm (Table S4) indicate that the closest fits to the adsorption data at 25, 40, and 55 °C are produced by ARE, χ^2, and HYBRID parameter sets, respectively. For this temperature sequence, the maximum adsorption capacity q_m of SA-MNP toward D2EHPA reduces from 346.2 ± 15.7 to 322.8 ± 17.1 and then 293.3 ± 15.6 mg.g^{-1}. Moreover, the Dubinin-Radushkevich constant K_{D-R} is correspondingly determined to be $(2.89 \pm 0.44) \times 10^{-8}$, $(2.87 \pm 0.52) \times 10^{-8}$, and $(3.68 \pm 0.66) \times 10^{-8}$ mol^2.kJ^{-2}, analogous to the mean free adsorption energies of 4.162 ± 0.317, 4.172 ± 0.378, and 3.686 ± 0.330 kJ.mol^{-1} (E, according to Equation (11)). The variations of saturation capacities and mean free energies imply the exothermic nature of D2EHPA adsorption, proceeding more efficiently at lower temperatures. The obtained energy values ($E < 8$ kJ.mol^{-1}) refer to the physical type of all adsorptions studied, according to the Dubinin-Radushkevich basic principles.

$$E = \frac{1}{\sqrt{2K_{D-R}}} \tag{11}$$

Fig. 8 collectively represents the application of the investigated isotherm models to the experimental D2EHPA adsorption data at different temperatures. Each model has been plotted based on its aforementioned optimum isotherm parameter set, which led to the minimal SNE value, according to Tables S1 to S4. In order to comparatively evaluate the fitting quality of various isotherm models to the equilibrium adsorption data, their corresponding error functions are listed in Table 2. Comparing diverse error functions reveals that the Langmuir isotherm model best describes the equilibrium D2EHPA adsorption onto SA-MNP at all three temperatures, as it leads to the slightest error values of any type, among others.

As the preparation of D2EHPA-functionalized nanoadsorbents follows the Langmuir model, this isotherm's theoretical principles and basic assumptions apply well to the process. Indeed, it can be deduced that the surface of stearate-modified magnetite nanoparticles is energetically homogeneous, and D2EHPA molecules form a monolayer surface coverage on it due to Van der Waals interactions with the identical adsorption sites available. Furthermore, as a critical advantage from the adsorption viewpoint, it is possible to estimate the extent of organic extractant present on the surface of nanoadsorbents. Fractional surface coverage is the intended parameter obtained by dividing the equilibrium uptake of the adsorbent material by the maximum theoretical adsorption capacity (q_e/q_m), according to the Langmuir isotherm model. This parameter influences the subsequent applications of the nanoadsorbents and can be manipulated during their fabrication procedure simply by tuning the extractant concentration in the solution. It is worth mentioning that fractional surface coverage resembles the extractant
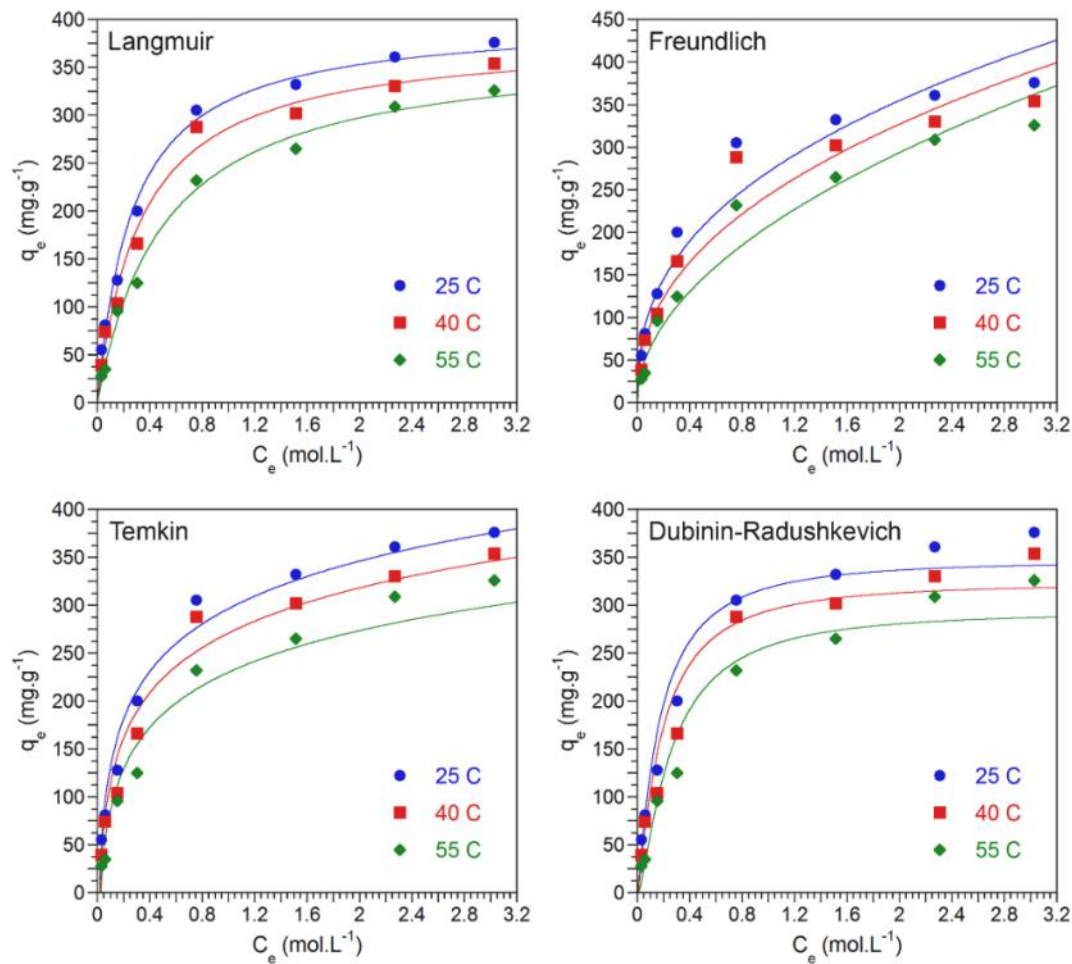
Fig. 8. Comparison of various isotherm models with the experimental data for D2EHPA adsorption onto SA-MNP at 25, 40, and 55 °C. The models are plotted based on their optimum constants.

Table 2
Error functions corresponding to the minimal SNE value for different adsorption isotherm models.

Temperature (°C)	Error function	Adsorption isotherm model			
		Langmuir	Freundlich	Temkin	Dubinin-Radushkevich
25	RMSE	10.6386	29.6572	17.2884	24.8004
	ERRSQ	905.4351	7036.3886	2391.1026	4920.4952
	MPSD	12.8965	16.4380	15.2041	19.7311
	ARE	7.8586	11.6735	9.8445	11.9641
	$\chi 2$	9.1655	30.1552	14.5520	27.4487
	HYBRID	132.8289	457.8630	268.1596	477.1209
40	RMSE	13.7545	30.5742	20.8286	26.7241
	ERRSQ	1513.4980	7478.2321	3470.6589	5713.4360
	MPSD	13.9553	20.7859	18.4548	23.5399
	ARE	9.8446	12.6572	11.4918	15.5860
	$\chi 2$	11.6738	35.8098	20.2763	31.9839
	HYBRID	179.1871	529.5820	393.1191	632.4655
55	RMSE	9.5062	24.5922	21.6028	23.0014
	ERRSQ	722.9498	4838.2198	3733.4485	4232.5057
	MPSD	13.6262	24.4323	36.4383	30.4995
	ARE	9.1760	16.8263	23.2355	17.0087
	$\chi 2$	6.9834	29.9827	53.1131	52.3200
	HYBRID	107.2648	476.4481	624.9755	532.2827

concentration in hydrometallurgical solvent extraction systems, which is vital for determining organometallic complexes and extraction mechanisms through the well-known slope analysis method [40,41].

4.3. Adsorption thermodynamics

In thermodynamic analysis based on the Van't Hoff relation (refer to Equation (8)), the adsorption equilibrium constant K_{ads} should be extracted from the best-fitted isotherm model's constant. The Langmuir isotherm model best describes the process of D2EHPA adsorption onto

the surface of SA-MNP at all intended temperatures (25, 40, and 55 °C). For adsorption of non-ionic constituents (D2EHPA extractant includes) obeying the Langmuir isotherm model, the K_{ads} is numerally equivalent to the Langmuir constant K_L in the L.mol^{-1} unit [38,39]. Hence, the relevant dimension problem is resolved by considering the unitary standard concentration of the adsorbate (1 mol.L^{-1}). The thermodynamic parameters are extracted according to the Van't Hoff plot (refer to Fig. S1 of the Supplementary Information), whose linearity is considered satisfactory due to the coefficient of determination (R^2) value of 0.96.

The negative value of $\Delta H°_{ads} = -17.3 \pm 3.7$ kJ.mol^{-1} confirms that D2EHPA adsorption onto SA-MNP is an exothermic process, as was previously suggested based on various interpretations. According to Atkins [42], the enthalpy change value is of an order of magnitude ($<$ 20 kJ.mol^{-1}) corresponding to D2EHPA physisorption. Expectedly, the negative value of $\Delta S°_{ads} = -46.6 \pm 11.6$ J.mol^{-1}.K^{-1} shows that system disorder and randomness diminish during the adsorption process as adsorbate constituents in the liquid phase are immobilized on the solid surface of the adsorbent material.

5. Conclusions

This study aimed to investigate the preparation of D2EHPA-functionalized superparamagnetic nanoadsorbents from an adsorption point of view. The 15 nm single-domain structure magnetite nanoparticles were synthesized through the co-precipitation method and chemically surface-modified with stearic acid through a carboxylate chelating bidentate mechanism. Finally, a monolayer D2EHPA extractant was physically adsorbed via Van der Waals interactions to the surface of stearate-modified nanoparticles. The superparamagnetic state of the nanoparticles and resultant nanoadsorbents was authenticated by the VSM analysis. However, non-magnetic organic layers surrounding the nanoparticles decreased the saturation magnetization from 62 to 48 emu.g^{-1} but was still sufficient for facile magnetic separation. D2EHPA stabilization on the surface of nanoadsorbents was qualitatively and quantitatively confirmed by the FT-IR and TGA techniques, respectively.

The nanoadsorbents' preparation process was thoroughly cognized from the adsorption viewpoint under different temperatures and D2EHPA concentrations. A comprehensive statistical analysis based on the non-linear regression method indicated that equilibrium D2EHPA physisorption onto SA-MNP was best described by the Langmuir isotherm model, suggesting that the extractant molecules formed a monolayer coverage on the energetically homogeneous stearate-modified magnetite nanoparticles. The maximum loading capacity of SA-MNP toward D2EHPA decreased from 400.1 to 382.3 and then 373.1 mg.g^{-1} by temperature rising from 25 to 40 and 55 °C, respectively. Thermodynamic investigations according to the Van't Hoff plot revealed that D2EHPA adsorption onto SA-MNP was an exothermic physical process ($\Delta H°_{ads} = -17.3$ kJ.mol^{-1}) which diminished the system randomness ($\Delta S°_{ads} = -46.6$ J.mol^{-1}.K^{-1}) and proceeded favorably.

CRediT authorship contribution statement

Farzad Firouzi: Conceptualization, Methodology, Investigation, Formal analysis, Data curation, Writing – original draft, Visualization. **Ali Nemati:** Supervision, Validation, Writing – review & editing. **Sayed Khatiboleslam Sadrnezhaad:** Supervision, Validation, Writing – review & editing.

Declaration of competing interest

The authors declare that they have no known competing financial interests or personal relationships that could have appeared to influence the work reported in this paper.

Data availability

The authors confirm that the data supporting the findings of this research are available within the paper and its supplementary information.

Appendix A. Supplementary material

Supplementary data to this article can be found online at https://doi.org/10.1016/j.molliq.2024.124069.

References

[1] R. Banda, M.S. Lee, Solvent extraction for the separation of Zr and Hf from aqueous solutions, Sep. Purif. Rev. 44 (3) (2015) 199–215, https://doi.org/10.1080/15422119.2014.920876.

[2] H.-S. Yoon, et al., Solvent extraction, separation and recovery of dysprosium (Dy) and neodymium (Nd) from aqueous solutions: Waste recycling strategies for permanent magnet processing, Hydrometall. 165 (2016) 27–43, https://doi.org/10.1016/j.hydromet.2016.01.028.

[3] A.B. Botelho Junior, D.B. Dreisinger, D.C. Espinosa, A review of nickel, copper, and cobalt recovery by chelating ion exchange resins from mining processes and mining tailings, Min., Metall. Exploration 36 (2019) 199–213, https://doi.org/10.1007/s42461-018-0016-8.

[4] J.-C. Lee, et al., Separation of platinum, palladium and rhodium from aqueous solutions using ion exchange resin: A review, Sep. Purif. Technol. 246 (2020) 116896, https://doi.org/10.1016/j.seppur.2020.116896.

[5] S. Wadhawan, et al., Role of nanomaterials as adsorbents in heavy metal ion removal from waste water: A review, J. Water Process Eng. 33 (2020) 101038, https://doi.org/10.1016/j.jwpe.2019.101038.

[6] Z. Ajmal, et al., Use of nano-/micro-magnetite for abatement of cadmium and lead contamination, J. Environ. Manage. 264 (2020) 110477, https://doi.org/10.1016/j.jenvman.2020.110477.

[7] G. Qu, et al., Thiol-functionalized multi-walled carbon nanotubes for effective removal of Pb(II) from aqueous solutions, Mater. Chem. Phys. 278 (2022) 125688, https://doi.org/10.1016/j.matchemphys.2021.125688.

[8] L. Nuñez, B. Buchholz, G. Vandegrift, Waste remediation using in situ magnetically assisted chemical separation, Sep. Sci. Technol. 30 (7–9) (1995) 1455–1471, https://doi.org/10.1080/01496399508010357.

[9] J. Hristov, L. Fachikov, An overview of separation by magnetically stabilized beds: State-of-the-art and potential applications, China Particuol. 5 (1–2) (2007) 11–18, https://doi.org/10.1016/j.cpart.2007.01.010.

[10] K. Petcharoen, A. Sirivat, Synthesis and characterization of magnetite nanoparticles via the chemical co-precipitation method, Mater. Sci. Eng. B 177 (5) (2012) 421–427, https://doi.org/10.1016/j.mseb.2012.01.003.

[11] V. Ganesan, et al., Size-controlled synthesis of superparamagnetic magnetite nanoclusters for heat generation in an alternating magnetic field, J. Mol. Liq. 281 (2019) 315–323, https://doi.org/10.1016/j.molliq.2019.02.095.

[12] L.B. Tahar, M.H. Oueslati, M.J.A. Abualreish, Synthesis of magnetite derivatives nanoparticles and their application for the removal of chromium (VI) from aqueous solutions, J. Colloid Interface Sci. 512 (2018) 115–126, https://doi.org/10.1016/j.jcis.2017.10.044.

[13] S. Liu, et al., Preparation, surface functionalization and application of Fe3O4 magnetic nanoparticles, Adv. Colloid Interface Sci. 281 (2020) 102165, https://doi.org/10.1016/j.cis.2020.102165.

[14] J. You, et al., A review of amino-functionalized magnetic nanoparticles for water treatment: Features and prospects, J. Clean. Prod. 281 (2021) 124668, https://doi.org/10.1016/j.jclepro.2020.124668.

[15] B. García-Merino, E. Bringas, I. Ortiz, Synthesis and applications of surface-modified magnetic nanoparticles: progress and future prospects, Rev. Chem. Eng. 38 (7) (2022) 821–842, https://doi.org/10.1515/revce-2020-0072.

[16] A.V. Samrot, et al., Surface-engineered super-paramagnetic iron oxide nanoparticles for chromium removal, Int. J. Nanomed. (2019) 8105–8119, https://doi.org/10.2147/IJN.S214236.

[17] S. Agarwal, et al., Mo (IV) adsorption from nitric acid media by Di-(2-ethylhexyl) phosphoric acid (D2EHPA) coated silanized magnetite nanoparticles, J. Mol. Liq. 218 (2016) 346–353, https://doi.org/10.1016/j.molliq.2016.02.057.

[18] L. Molina, et al., Synthesis and characterization of magnetite nanoparticles functionalized with organophosphorus compounds and its application as an adsorbent for La (III), Nd (III) and Pr (III) ions from aqueous solutions, J. Mol. Liq. 275 (2019) 178–191, https://doi.org/10.1016/j.molliq.2018.11.074.

[19] C. Basualto, et al., Lanthanide sorbent based on magnetite nanoparticles functionalized with organophosphorus extractants, Sci. Technol. Adv. Mater. (2015), https://doi.org/10.1088/1468-6996/16/3/035010.

[20] T. Burks, et al., Removal of chromium (VI) using surface modified superparamagnetic iron oxide nanoparticles, Sep. Sci. Technol. 48 (8) (2013) 1243–1251, https://doi.org/10.1080/01496395.2012.734364.

[21] D. Wu, Y. Sun, Q. Wang, Adsorption of lanthanum (III) from aqueous solution using 2-ethylhexyl phosphonic acid mono-2-ethylhexyl ester-grafted magnetic silica nanocomposites, J. Hazard. Mater. 260 (2013) 409–419, https://doi.org/10.1016/j.jhazmat.2013.05.042.

[22] L. Zhang, et al., Adsorption and selective separation of neodymium with magnetic alginate microcapsules containing the extractant 2-ethylhexyl phosphonic acid mono-2-ethylhexyl ester, J. Chem. Eng. Data 56 (5) (2011) 2280–2289, https://doi.org/10.1021/je101270j.

[23] Z.F. Akl, Theoretical and experimental studies on uranium (vi) adsorption using phosphine oxide-coated magnetic nanoadsorbent, RSC Adv. 11 (62) (2021) 39233–39244, https://doi.org/10.1039/D1RA04515F.

[24] M. Aliakbari, et al., Separation of hafnium and zirconium using TBP modified ferromagnetic nanoparticles: Effects of acid and metals concentrations, Hydrometall. 146 (2014) 72–75, https://doi.org/10.1016/j.hydromet.2014.03.002.

[25] A. Behnam-Saba, et al., A Chemometric Study of the Adsorption of Zr (IV) Ions from Aqueous Solutions onto TBP-Surface-Modified Magnetic Fe3O4 Nanoparticles as a New Adsorbent, Radiochemistry 62 (1) (2020) 62–72, https://doi.org/10.1134/S1066362220010087.

[26] M.S.A. Darwish, Effect of carriers on heating efficiency of oleic acid-stabilized magnetite nanoparticles, J. Mol. Liq. 231 (2017) 80–85, https://doi.org/10.1016/j.molliq.2017.01.094.

[27] P.I.P. Soares, et al., Iron oxide nanoparticles stabilized with a bilayer of oleic acid for magnetic hyperthermia and MRI applications, Appl. Surf. Sci. 383 (2016) 240–247, https://doi.org/10.1016/j.apsusc.2016.04.181.

[28] M.-J. Chen, et al., Magnetic fluids' stability improved by oleic acid bilayer-coated structure via one-pot synthesis, Chem. Pap. 70 (12) (2016) 1642–1648, https://doi.org/10.1515/chempap-2016-0096.

[29] L. Zhang, R. He, H.-C. Gu, Oleic acid coating on the monodisperse magnetite nanoparticles, Appl. Surf. Sci. 253 (5) (2006) 2611–2617, https://doi.org/10.1016/j.apsusc.2006.05.023.

[30] M.H. Wood, et al., Comparative adsorption of saturated and unsaturated fatty acids at the iron oxide/oil interface, Langmuir 32 (2) (2016) 534–540, https://doi.org/10.1021/acs.langmuir.5b04435.

[31] J.R. Kanicky, D.O. Shah, Effect of Degree, Type, and Position of Unsaturation on the pKa of Long-Chain Fatty Acids, J. Colloid Interface Sci. 256 (1) (2002) 201–207, https://doi.org/10.1006/jcis.2001.8009.

[32] J. Wang, X. Guo, Adsorption isotherm models: Classification, physical meaning, application and solving method, Chemosphere 258 (2020) 127279, https://doi.org/10.1016/j.chemosphere.2020.127279.

[33] M.A. Al-Ghouti, D.A. Da'ana, Guidelines for the use and interpretation of adsorption isotherm models: A review, J. Hazard. Mater. 393 (2020) 122383, https://doi.org/10.1016/j.jhazmat.2020.122383.

[34] C. Comuzzi, et al., SOLVERSTAT: a new utility for multipurpose analysis. An application to the investigation of dioxygenated Co(II) complex formation in dimethylsulfoxide solution, Talanta 59 (1) (2003) 67–80, https://doi.org/10.1016/S0039-9140(02)00457-5.

[35] S. Kundu, A.K. Gupta, Arsenic adsorption onto iron oxide-coated cement (IOCC): regression analysis of equilibrium data with several isotherm models and their optimization, Chem. Eng. J. 122 (1–2) (2006) 93–106, https://doi.org/10.1016/j.cej.2006.06.002.

[36] F. Gimbert, et al., Adsorption isotherm models for dye removal by cationized starch-based material in a single component system: error analysis, J. Hazard. Mater. 157 (1) (2008) 34–46, https://doi.org/10.1016/j.jhazmat.2007.12.072.

[37] K.Y. Foo, B.H. Hameed, Insights into the modeling of adsorption isotherm systems, Chem. Eng. J. 156 (1) (2010) 2–10, https://doi.org/10.1016/j.cej.2009.09.013.

[38] E.C. Lima, et al., A critical review of the estimation of the thermodynamic parameters on adsorption equilibria. Wrong use of equilibrium constant in the Van't Hoof equation for calculation of thermodynamic parameters of adsorption, J. Mol. Liq. 273 (2019) 425–434, https://doi.org/10.1016/j.molliq.2018.10.048.

[39] P.S. Ghosal, A.K. Gupta, Determination of thermodynamic parameters from Langmuir isotherm constant-revisited, J. Mol. Liq. 225 (2017) 137–146, https://doi.org/10.1016/j.molliq.2016.11.058.

[40] E. Makombe, et al., Uranium(VI) and thorium(IV) extraction by malonamides: Impact of ligand molecular topology on selectivity, J. Mol. Liq. 368 (2022) 120701, https://doi.org/10.1016/j.molliq.2022.120701.

[41] S. Alizadeh, et al., Nitrate ions effects on solvent extraction of rare earth elements from aqueous solutions by D2EHPA: Experimental studies and molecular simulations, J. Mol. Liq. 333 (2021) 116015, https://doi.org/10.1016/j.molliq.2021.116015.

[42] P. Atkins, Physical chemistry, 6th ed., Oxford University Press, London, 1999.